processes

MDPI

Article

Numerical Study of the Effects of Roughness Coupled with Inclination on a Turbulent Flow around an Obstacle

Amine Brahimi [1,2], Redha Rebhi [1,2] and Mounir Alliche [1,2,*]

[1] LERM—Renewable Energy and Materials Laboratory, University of Medea, Medea 26000, Algeria; ami_brahimi@yahoo.fr (A.B.); rebhi.redha@gmail.com (R.R.)
[2] Department of Mechanical Engineering, Faculty of Technology, University of Medea, Medea 26000, Algeria
* Correspondence: alliche.mounir@univ-medea.dz

Abstract: In this study, we simulate the cooling of a microprocessor by thermal convection in three different shapes: a square, a trapezoidal, and a triangular shape. The latter is improved by a variety of types of roughness, including square roughness, triangular roughness Type 1, triangular roughness Type 2, and triangular roughness Type 3. The microprocessors are kept at a constant temperature, the air flow is constant, and the geometry is fixed. The physical phenomenon is simulated by the ANSYS software. The numerical results reported in this study cover the ranges of the obstacle's angle of inclination, $0° \leq \theta \leq 45°$, (square obstacles, $\theta = 0°$, trapezoidal obstacles, $0° < \theta < 45°$, triangular obstacles, $\theta = 45°$) and Reynolds number, $2500 \leq Re \leq 10,000$. The findings relate to streamlines, dynamic pressure (max), mean velocity, temperature field, mean Nusselt number (Nu/Nu_0) profiles, local coefficient of friction (Cf/f_0), mean coefficient of friction (f/f_0) profiles, mean velocity field with roughness, and fluid temperature field with roughness. The aim of the study is to show the interaction between the roughness parameter and the obstacle geometry. In the case of a triangular obstacle, the contact between the cold air and the obstacle is significant downstream of the obstacle, which gives us good cooling, and the Nusselt number has an important value because the agitation of the flow increases convective heat transfer, and the coefficient of friction is low because the air flow is uniform.

Keywords: forced convection; obstacle; CFD; roughness; Nusselt numbers; friction

Citation: Brahimi, A.; Rebhi, R.; Alliche, M. Numerical Study of the Effects of Roughness Coupled with Inclination on a Turbulent Flow around an Obstacle. *Processes* **2023**, *11*, 1979. https://doi.org/10.3390/pr11071979

Academic Editor: Ireneusz Zbicinski

Received: 5 June 2023
Revised: 20 June 2023
Accepted: 25 June 2023
Published: 30 June 2023

1. Introduction

Currently, forced or free convection environments are used to cool personal computers. The most common cooling methods for greater or lower heat flows involve fans attached to the central processing unit. However, due to a number of factors, including the size of the workspace, the noise, and the quality of the limit cooling, these cooling systems have some limitations for electronic components that operate at higher frequencies (over 1000 megahertz). As a result, novel cooling techniques must be used to dissipate thermal energy greater than 100 W/cm^2 from an electronic component's surface while keeping the device (or component) at acceptable temperatures, usually below 85 °C. In order to accelerate the rate of heat transmission, impediments are placed in the channel's duct to induce turbulence. Baffles and fins are positioned in the forced flow to create secondary currents or recirculation zones in order to produce turbulence. These are employed to enhance heat transfer in a number of engineering applications, such as solar channels and heat exchangers [1]. The improvement of heat transmission and pressure drop caused by connecting barrier elements of various shapes, sizes, inclinations, and orientations to the channel walls has been investigated by several researchers [2–6] using experimental approaches. Their findings demonstrate that the Nusselt number and thermal efficiency were raised by experimental and numerical analyses to improve thermal performance. The characterization of the air pressure and velocity field inside a rectangular duct with two baffle plates installed on opposing sides was provided by Demartini et al. [7]. Baffle

plates are found in shell and tube heat exchangers, and the geometry of the problem is a simplification of that geometry. The extent of the low-pressure regions in the downstream regions and the high-pressure regions generated upstream of both baffle plates are the most significant aspects seen. Cao et al. [8] and Saedodin et al. [9] used the lattice Boltzmann method and Abchouyeh et al. [10] carried out a numerical investigation of a horizontal sinusoidal baffle channel containing a water/Cu nanofluid. They claimed that when the nanoparticle fraction and obstacle space increased, so did the average Nusselt number values. According to the findings, the wedge ribs significantly improved heat transfer and pressure drop. Chompookham et al. [11] offer two types of triangular ribs. Using inclined solid and perforated baffles with a Reynolds number of 12,000 to 41,000, two equally sized baffles were introduced into a rectangular channel by Dutta and Hossain [12], increasing the local heat transfer characteristics as well as the friction through the channel. The findings show that the local Nusselt number has a considerable impact on the orientation, location, and shape of the second deflector. A flat plate solar air heater's energy and exergy analyses were shown by Kalaiarasi et al. [13]. In order to increase thermal efficiency, Peng et al. [14] demonstrated a new kind of solar air collector that uses finned pins on its absorber. Selimefendigil et al. [15] performed a computational analysis of the hydrothermal properties of the convective laminar nanofluid Fe_3O_4 through a bifurcating type channel with a changeable magnetic field based on the finite element method in addition to experimental methods. Through a square pipe with various baffles, including trapezoidal, triangular, and square shapes, Kamali and Binesh [16] explored turbulent heat transmission and examined friction properties. A baffle was inserted by Nasiruddin et al. [17] to enhance heat transfer inside a circular tube. The effect of the baffles' size and position on the channel's thermal performance was investigated. Pin fins were installed by Wang et al. [18] to enhance heat transfer in a rectangular channel. The properties of forced convection heat transfer in the presence of transverse grooves on the bottom surface of a two-dimensional channel were reported by Eiamsa-ard and Promvonge [19]. With the use of circular section rings with various spacings, Ozceyhan et al.'s [20] simulation of heat transmission and friction in a tube was accomplished. FLUENT was used to run the simulation, and the Reynolds values ranged from 4475 to 43,725. In a square channel with discrete type "V" baffles, Promvonge et al. [21] simulate a turbulent flow and heat transfer in three dimensions. This simulation made use of the finite volume approach and the SIMPLE algorithm. In a two-dimensional channel, the effects of introducing diamond-shaped baffles with various tip angles on thermal enhancement were examined statistically by Sripattanapipat and Promvonge [22]. Yang [23] reviewed the development of LES applications in transitional flows and gas turbine combustor flows. There were several major challenges/issues associated with LES and its application such as SGS modeling, generation methods for inflow boundary conditions, wall layer modeling, LES of turbulent combustion, etc. He concluded that the LES will be undoubtedly the main tool for engineering fluid analysis within a couple of decades since DNS will still be far too expensive. In the future, LES is likely to be used for a broader range of flow problems and for more complex problems including more multi-disciplinary applications. De Vanna et al. [24] studied the physical reliability of turbulence modeling in an adverse pressure gradient wall flow setup at moderate/high Reynolds number. A canonical configuration of shockwave/boundary layer interaction is used to illustrate the wall modeling behavior. In particular, a standard equilibrium-based wall-modeling approach, combined with an innovative strategy to keep the no-slip velocity and adiabatic/isothermal temperature constraints at the wall, is adopted. The lattice Boltzmann method was used by Pirouz et al. [25] to model conjugate heat flow inside a rectangular channel with associated barriers. Mohammedi et al. [26] investigated how to increase heat transfer efficiency and outlet air temperature in a finned and baffled solar water heater. The enhancement of heat transfer inside a square duct fitted with oblique horseshoe baffles was explored by Skullong et al. [27]. When airflow and an absorber installed with corrugated fins were present, Priyam and Chand [28] investigated the effect of flow on the efficiency of a solar collector. To assess the internal flow and heat transfer properties of a solar air

collector with baffles, Hu et al. [29] used numerical analysis. Amraoui and Aliane [30] used the CFD technique to simulate the research of fluid flow and heat transfer in a solar channel with obstacles, while Amraoui [31] used CFX software to simulate the study of air flow around a circular obstacle field in an air CSP. The same author, Amraoui [32], conducted a three-dimensional evaluation of two different solar collector types more recently. To complete their research quickly and cheaply, they used the ANSYS simulation code. In order to improve efficiency, Amraoui and Benosman [33] incorporated square barriers. The height and pitch of the roughness element are the two most significant characteristics, although many other factors contribute to the arrangement and shape of the roughness components. Reynolds number, rib cross section, angle of attack, and combined turbulence promoters are further parameters. Using direct numerical simulations, Leonardi et al. [34] investigated the ordered motion of a turbulent flow in a channel with a series of square bars on the lower and upper sides. For the examination of heat transfer in a rough-walled conduit with sand grains and two-dimensional periodic square section ribs on a wall surface for turbulent flow, Miyake et al. [35] performed direct numerical simulations. The impact of repeated ribs on the thermal efficiency of a flat absorber plate solar air channel was investigated by Ansari and Bazargan [36]. After designing a ribbed rough surface for a channel, Kim and Kim [37] presented a study on the numerical optimization technique combined with RANS analysis of flow and heat transmission. A two-passage square channel with and without square section parallel ribs at a 90° angle on a wall surface was subjected to a 3D numerical simulation by Jang et al. [38]. With angular ribs extruded on two opposing surfaces, Kim and Kim [39] carried out a numerical simulation of fluid flow and heat transfer for channel shape optimization. In a triangular duct with ribs, Kumar et al. [40] looked into the flow and heat transmission characteristics. In the context of surface roughness effects, Ryu et al. [41] looked into the heat transfer characteristics of turbulent flow in channels with two-dimensional ribs and three-dimensional blocks. In order to analyze the heat transfer and hydraulic behavior of the fluid in a rectangular channel flow with periodic ribs installed on one of the major walls, Liu et al. [42] conducted a numerical and experimental investigation. To forecast the thermal–hydraulic performance of a solar air channel roughened with conical and spherical ribs, Alam and Kim [43] used numerical simulations. For the numerical optimization of the energy and exergy efficiency of a solar air channel with twisted rib roughness on a heating plate, Kumar and Layek [44] conducted a stochastic analysis. Skullong et al. [45] used corrugated grooves embedded with pairs of trapezoidal fins (ATs) positioned on the absorber plate to investigate the heat transfer properties in a solar air channel. In order to explore the heat transfer, friction factor, and thermal–hydraulic performance characteristics of flow in a rough rectangular duct, Deo et al. [46] carried out an experimental investigation. The thermal and hydraulic performance of a roughened, dual-flow solar air channel with several C-shaped ribs was experimentally investigated by Gabhane and Kanase-Patil [47]. An experimental investigation on heat transmission and coefficient of friction for a synthetically rough solar air duct was presented by Kumar et al. [48]. For the range of tested roughness parameters, it was discovered that a rough solar air duct performs better than a smooth duct. The experimental research of heat transmission and friction factor in a countercurrent double-pass solar air channel with a V-shaped discrete rib roughness and shifted over two substantial surfaces of the heated plate was reviewed by Ravi and Saini [49].

The numerical analysis of the turbulent air flow in forced convection around a barrier was of particular interest to us in this work. In order to validate this model, the outcomes were compared to those reported in the literature under similar circumstances. Our project used fluid calculation code to mimic the cooling of a microprocessor in two dimensions.

2. Methodology

The investigation revolved around a heat exchanger. It has a horizontal, rectangular channel, an isothermal upper wall, a thermally insulated lower wall, and extended

surfaces in the form of intermittently spaced-apart obstacles. Figure 1 presents a precise geometric illustration.

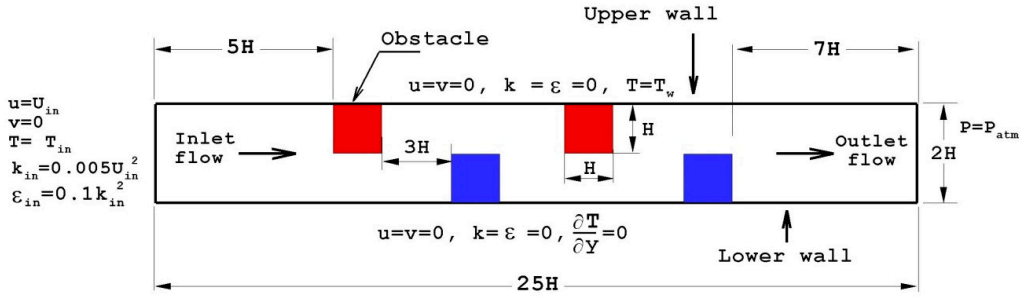

Figure 1. Geometry under investigation and boundary conditions.

In order to determine the ideal setting for enhanced heat transfer, we primarily concentrated on an essential geometric variable associated with an obstacle in the first section of this study, namely the effect of the slope of their leading edges. Figure 2 shows three cases that can occur depending on the leading edge of the obstacle's angle of inclination:

- Square obstacles in the case where: $\theta = 0°$;
- Trapezoidal obstacles in the case where: $0° < \theta < 45°$;
- Triangular obstacles in the case where: $\theta = 45°$.

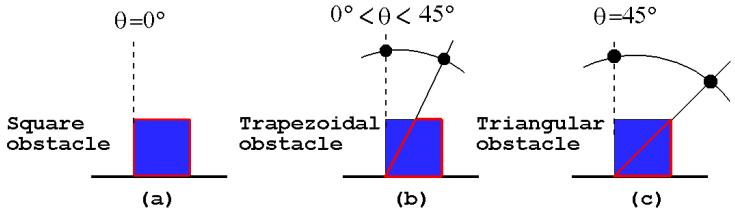

Figure 2. Different angles of inclination of the straight sides of obstacles: (**a**) $\theta = 0°$: square obstacle, (**b**) $0° < \theta < 45°$: trapezoidal obstacle, and (**c**) $\theta = 45°$: triangular obstacle.

To improve the performance of the heat exchanger channel, rough walls were used in the presence of fins and triangular baffles. The third model, Figure 2c is compared to the performances of four channels in the presence of four roughness modes: square, Figure 3a, triangular Type 1, Figure 3b, triangular Type 2, Figure 3c, and triangular Type 3, Figure 3d. In all the cases proposed, the roughness is present only on the upper hot wall of the channel, exactly in line with the last obstacle.

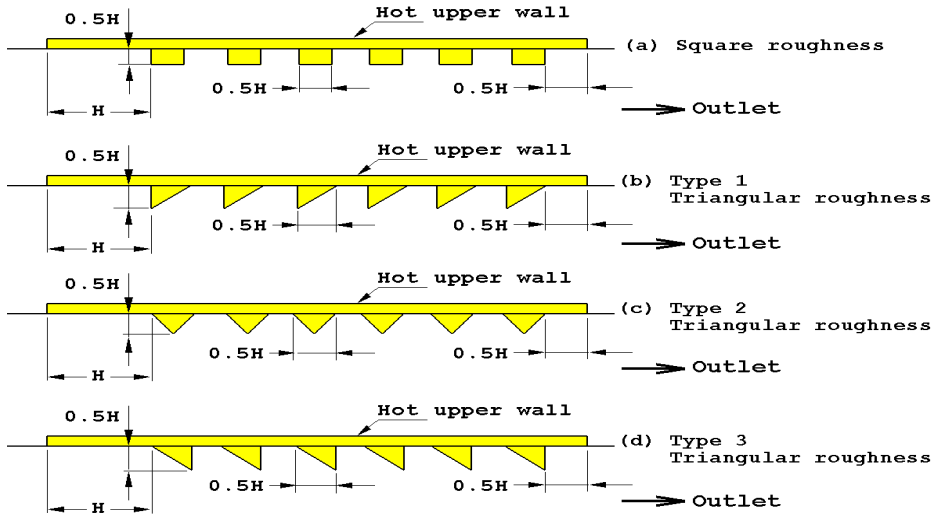

Figure 3. Various cases of roughness shapes.

The specific parameters of the geometry and the thermo-physical data of the fluid (air) and of the solid (walls) are indicated in Tables 1 and 2.

Table 1. Geometric parameters of heat exchanger channel with H = 0.01 m.

Dimension	H
Channel length	25 H
Channel height	2 H
Channel hydraulic diameter	2 H
Obstacle width	1 H
Obstacle height	1 H
Separation distance from obstacles	3 H
Roughness width	0.5 H
Roughness height	0.5 H
Distance between two roughness units	0.5 H
Distance between the channel entrance and the left side of the first obstacle	5 H
Distance between the right side of the last obstacle and the exit of the conduit	7 H
Distance from the right side of the last obstacle to the first roughness unit	1 H
Distance from the right side of the last roughness unit to the exit of the channel	0.5 H

Table 2. Thermo-physical data of air and Al at 300 K.

	k (W/m·K)	Cp (J/kg·K)	ρ (kg/m^3)	μ (Pa·s)	Pr
Air	0.0242	1006.43	1.225	1.7894×10^{-5}	0.71
Al	0.1672	14,283	0.08189	...	...

The aerodynamic and thermal boundary conditions were chosen according to the simulation of Nasiruddin and Kamran Siddiqui [17] as shown in Figure 1.

At the inlet $(x = 0, 0 \leq y \leq 2H)$:

$$\left.\begin{array}{c} u(0,y) = U_{in} \\ v(0,y) = 0 \\ T(0,y) = T_{in} \\ k(0,y) = k_{in} = 0.005 \times U_{in}^2 \\ \varepsilon(0,y) = \varepsilon_{in} = 0.1 \times k_{in}^2 \end{array}\right\} \quad (1)$$

At the outlet $(x = 25H, 0 \leq y \leq 2H)$:

$$\left.\begin{array}{c} P(L,y) = P_{atm} \\ \frac{\partial \varnothing}{\partial x}(L,y) = 0 \end{array}\right\} \quad (2)$$

where $\phi \equiv (u, v, T, k, \varepsilon)$.

At the upper surface $(0 \leq x \leq 25H, y = 2H)$:

$$\left.\begin{array}{c} u = v = 0 \\ k = \varepsilon = 0 \\ T = T_w \end{array}\right\} \quad (3)$$

At the lower surface $(0 \leq x \leq 25H, y = 0)$:

$$\left.\begin{array}{c} u = v = 0 \\ k = \varepsilon = 0 \\ \frac{\partial T}{\partial y} = 0 \end{array}\right\} \quad (4)$$

At the solid/fluid interface, the following condition is applied:

$$\left.\begin{array}{c} T_s = T_f \\ \lambda_S \frac{\partial T_s}{\partial n}\Big|_{\vec{N}} = \lambda_f \frac{\partial T_f}{\partial n}\Big|_{\vec{N}} \end{array}\right\} \quad (5)$$

where $\vec{N}$ is the vector normal to the considered surface interface, λ_S and λ_f are thermal conductivities of solid and fluid, respectively.

The computational domain fitted with square obstacle, trapezoidal obstacle, and triangular obstacle was simulated using the computational fluid dynamics (CFD) commercial software ANSYS Fluent.

The $k-\varepsilon$ turbulence was adopted in this study. In Cartesian coordinates, the continuity, momentum, energy, and turbulence equations can be written in the following compact form Patankar [50]:

$$\frac{\partial}{\partial x}(\rho u\phi) + \frac{\partial}{\partial x}(\rho v\phi) = \frac{\partial}{\partial x}\left[E_\phi \frac{\partial \phi}{\partial x}\right] + \frac{\partial}{\partial y}\left[E_\phi \frac{\partial \phi}{\partial y}\right] + S_\phi \Bigg\} \quad (6)$$

where ϕ is a variable that serves to represent quantities such as the velocity components u and v, the turbulent kinetic energy k or the rate of turbulent energy dissipation ε, and the temperature T. However, the diffusion coefficient E_ϕ and the source term S_ϕ have specific values for the different conservation equations in the case of the standard $k-\varepsilon$ turbulence model.

Continuity equation

$$\left.\begin{array}{c} \varnothing = 1 \\ E_\phi = 0 \\ S_\phi = 0 \end{array}\right\} \quad (7)$$

Momentum equation in X-direction

$$\left.\begin{array}{c} \varnothing = u \\ E_\phi = \mu_e \\ S_\phi = -\frac{\partial P}{\partial x} + \frac{\partial}{\partial x}\left[\mu_e\left(\frac{\partial u}{\partial x}\right)\right] + \frac{\partial}{\partial y}\left[\mu_e\left(\frac{\partial v}{\partial x}\right)\right] \end{array}\right\} \quad (8)$$

Momentum equation in Y-direction

$$\left.\begin{array}{l} \varnothing = v \\ E_\phi = \mu_e \\ S_\phi = -\frac{\partial P}{\partial y} + \frac{\partial}{\partial x}\left[\mu_e\left(\frac{\partial u}{\partial x}\right)\right] + \frac{\partial}{\partial y}\left[\mu_e\left(\frac{\partial v}{\partial x}\right)\right] \end{array}\right\} \quad (9)$$

Conservation of energy in the fluid region

$$\left.\begin{array}{c} \varnothing = T \\ E_\phi = \frac{\mu_e}{\sigma_T} \\ S_\phi = 0 \end{array}\right\} \quad (10)$$

Conservation of energy in the solid region

$$\left.\begin{array}{l} \varnothing = T \\ E_\phi = \lambda_S \\ S_\phi = \frac{\partial}{\partial x}(\rho_s u T) + \frac{\partial}{\partial y}(\rho_s v T) \end{array}\right\} \quad (11)$$

k-Turbulent kinetic energy equation

$$\left.\begin{array}{c} \varnothing = k \\ E_\phi = \mu_l + \frac{\mu_t}{\sigma_k} \\ S_\phi = -\rho\varepsilon + G_k \end{array}\right\} \tag{12}$$

ε-Turbulent dissipation rate equation

$$\left.\begin{array}{l} \varnothing = \varepsilon \\ E_\phi = \mu_l + \frac{\mu_t}{\sigma_\varepsilon} \\ S_\phi = \frac{\varepsilon}{k}(C_{1\varepsilon}G_k - C_{2\varepsilon}\rho\varepsilon) \end{array}\right\} \tag{13}$$

G_k is the rate of kinetic energy production due to energy transfer from the turbulent mean flow; it is given by:

$$\left.\begin{array}{c} \mu_{eff} = \mu_l + \mu_t \\ G_k = \mu_t\left\{2\left[\left(\frac{\partial u}{\partial x}\right)^2 + \left(\frac{\partial v}{\partial y}\right)^2\right] + \left(\frac{\partial u}{\partial y} + \frac{\partial v}{\partial x}\right)^2\right\} \end{array}\right\} \tag{14}$$

where $C_\mu = 0.09$; $C_{1\varepsilon} = 1.44$; $C_{2\varepsilon} = 1.92$; $\sigma_k = 1.0$; $\sigma_\varepsilon = 1.3$, $\sigma_T = 0.9$ are the constants of the model, as proposed by Laundry and Spalding [50].

3. Results and Discussion

For the numerical simulations presented in this article, we refer to the experimental work of Demartini et al. [7], who studied planar baffles. Figure 4 shows our result and those obtained by Demartini et al. [7]. The three meshes tested (coarse: 97,593 nodes, medium: 215,897 nodes, and fine: 458,632 nodes) are illustrated in Figure 4. For turbulence models that use the wall functions equation, $k-\varepsilon$, the first cell is placed in the fully turbulent (log-law) region just after the buffer layer which satisfies the condition $y^+ \approx 30$. It depicts the pressure coefficient profiles with some previously studied numerical results for U_{in} = 7.8 m/s after the second chicane at x = 0.405 m. A good agreement between the numerical results, for fine mesh, and experimental results is observed, showing the growth of the pressure coefficient near the walls. The lower pressure values near the tip of the baffles are due to the high velocities in this region. Consequently, the fine mesh was chosen, despite the simulation being terminated due to excessive element distortion.

The evolution of the streamlines for the various types of obstacle with angles of $\theta = 0^\circ$, $0^\circ < \theta < 45^\circ$, and $\theta = 45^\circ$ is shown in Figure 5. According to the obstacle, we see that the streamlines alternate between the three forms, Figure 5a–c. The streamlines in Figure 5a (square obstacle) are less contoured as they cross the barrier, causing turbulence that disrupts the flow. The streamlines in Figure 5b, for the trapezoidal obstacle, straighten as they cross it, changing the streamlines' field direction. The streamlines are attached to the obstacle in Figure 5c, the triangular obstacle, giving us a powerful streamline field.

According to Figure 5, complex phenomena including recirculation zones and regions of turbulence upstream and downstream of the obstacle are produced by the flows in the air veins for the three different types of obstacle. The existence of impediments leads the three air streams to divide into multiple distinct zones above, below, and upstream of the obstructions. As a result, the flow creates recirculation zones (Zone A) close to the lower obstacles, which intensifies the turbulence upstream of the upper obstacles (Zone B). In addition to the separation of the fluid flow induced by the obstructions (Zone C), there are dead zones upstream of the lower obstacles (Zone C) plus the separation of the fluid flow caused by the obstacles. We observe that the importance of the dead zone for trapezoidal-shaped obstacles is less than that of square obstacles, and that it is almost zero for the model with triangular obstacles. When compared to previous models that have square and trapezoidal barriers, the model with triangle obstacles has a significantly large turbulent zone (Zone B). Figure 6 depicts dynamic pressure, which is the flow of

momentum per unit volume (the kinetic energy density). The three varieties under study are similar in terms of the overall dynamic pressure setup.

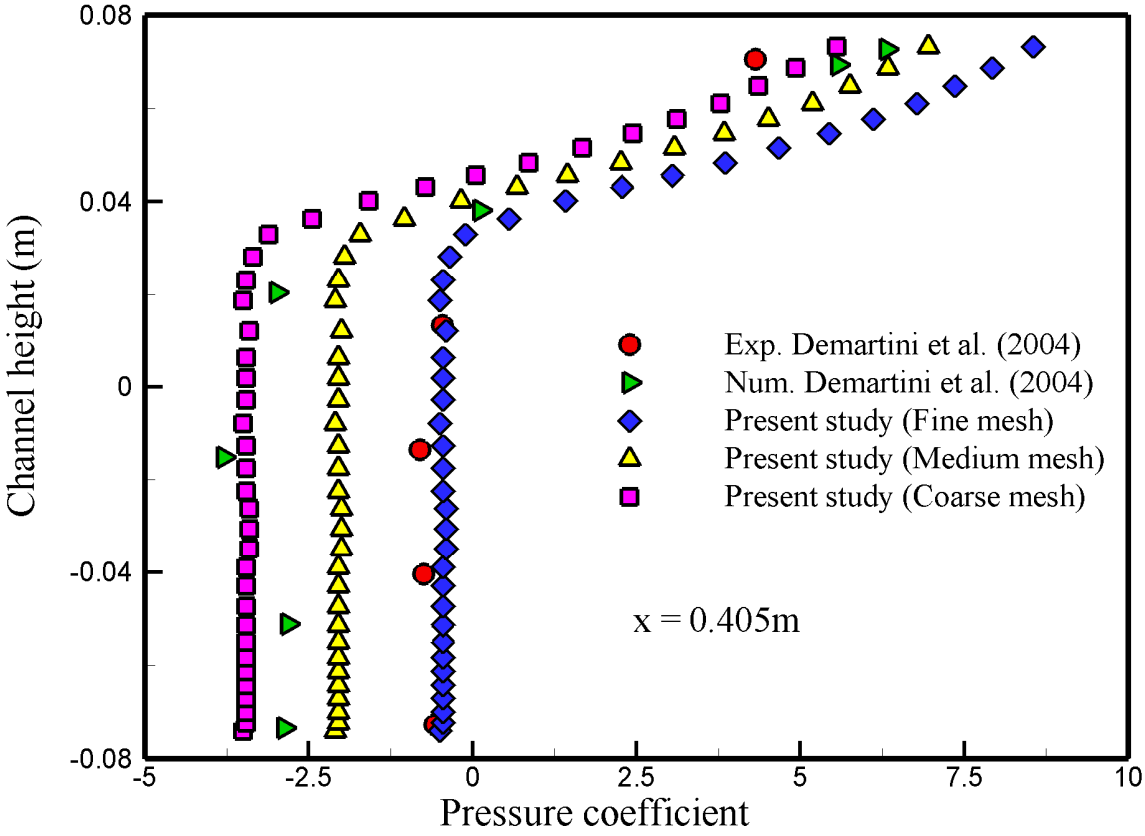

Figure 4. Comparison between the results of Demartini et al. [7] and present results for $U_{in} = 7.8$ m/s. Comparison between the results of (reprinted with permission from AIP Publishing, Copyright 2017) (a) and the present results.

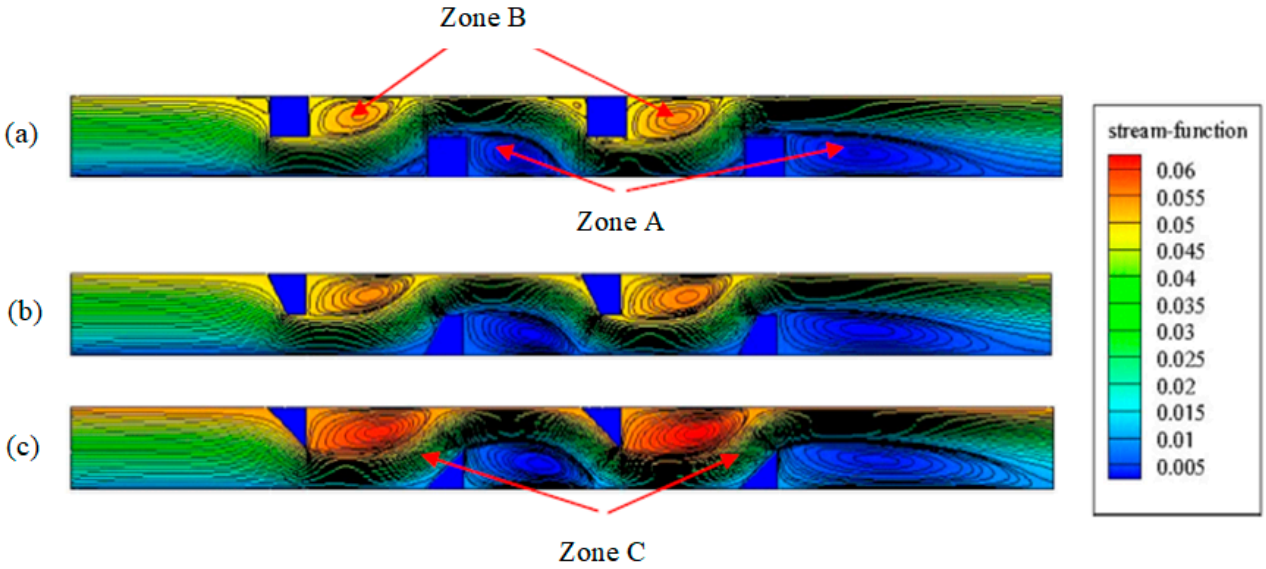

Figure 5. Streamlines for $Re = 2500$ and different obstacles: (**a**) $\theta = 0°$: square obstacle, (**b**) $0 < \theta < 45°$: trapezoidal obstacle, (**c**) $\theta = 45°$: triangular obstacle.

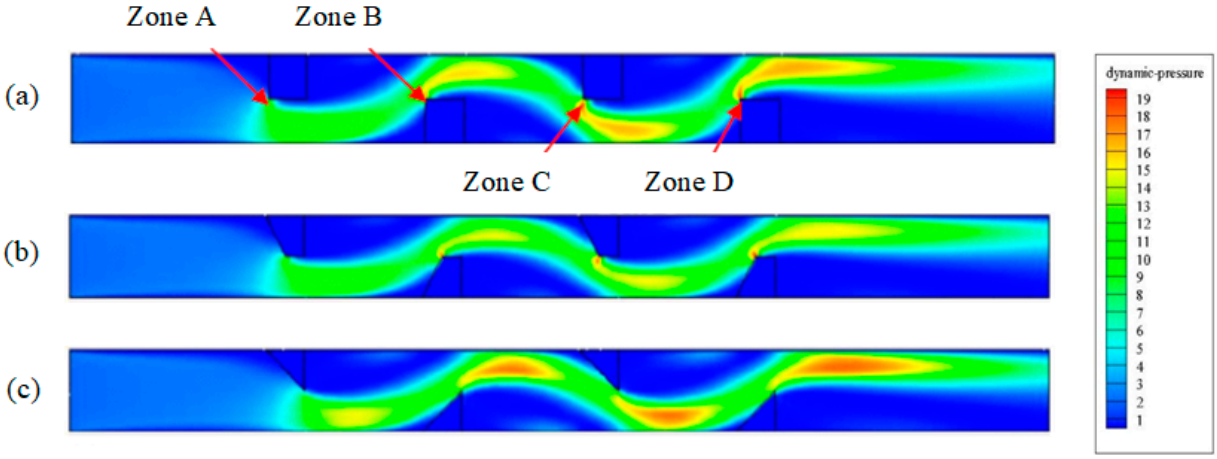

Figure 6. Contours of dynamic pressure fields for Re = 2500 and different angles of obstacles: (**a**) $\theta = 0°$: square obstacle; (**b**) $0° < \theta < 45°$: trapezoidal obstacle; and (**c**) $\theta = 45°$: triangular obstacle.

The dynamic pressure is uniform at the entrance, immediately below the first upper obstacle zone. Upstream of the upper and lower obstacles, the dynamic pressure approaches zero values. The zones (A, B, C, and D) with the highest dynamic pressure are separated by the sharp upstream edge. However, the flow separates from the obstacle's wall, which results in a depression downwind of these obstacles. Due to the poor circulation at this location, the dynamic pressure at the attack terminals in Figure 6a is nearly negligible. The dynamic pressure in Figure 6b must be displaced along the profile, causing an average flow of kinetic energy. The pressure in Figure 6c has a substantial value since the profile is ideal, which allowed for a large movement.

For the three types of obstacles, $0° < \theta < 45°$, Figure 7 shows the dynamic pressure fluctuation as a function of the Reynolds number (Re = 2500, 5000, 7500, and 10,000). Remember that pressure increases every time the Reynolds number increases. As can be seen, the pressure values for the square and trapezoidal obstacles are extremely close to each other. In addition, compared to the two preceding situations, the pressure value in the triangular case is relatively low.

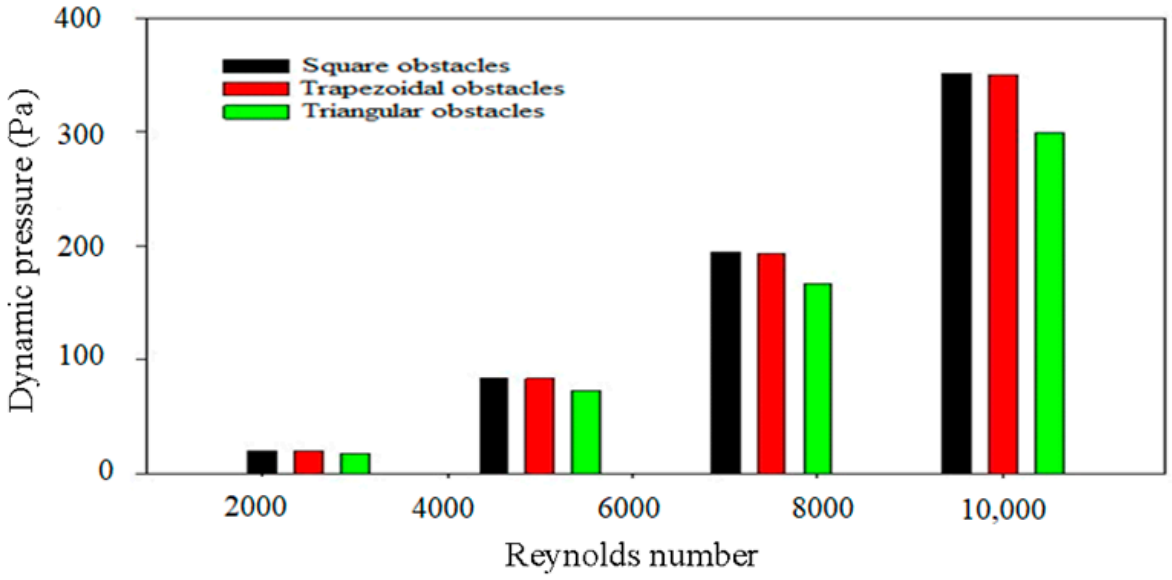

Figure 7. The effect of the inclination of the upstream edge of the obstacle on the dynamic pressure (max) for various values of the Reynolds number.

The entire distance traveled over a certain period of time divided by that period of time is the average velocity. The vortex is always created upstream of the rectangular obstacle, as seen in Figure 8. On the other hand, at the level of the triangular and trapezoidal obstacles, the flow consistently adheres to the obstacle's wall and follows it. As a result, the flow has two crucial moments. Figures clearly demonstrate that the ridge downstream of the obstacle has an impact on fluid behavior even upstream of it, altering how the flow interacts with the upper wall of the triangle obstacle. This enables us to claim that the presence of the inclination at the level of the edge upstream of the obstacle not only controls the zone of the triangle but also the area around this obstacle.

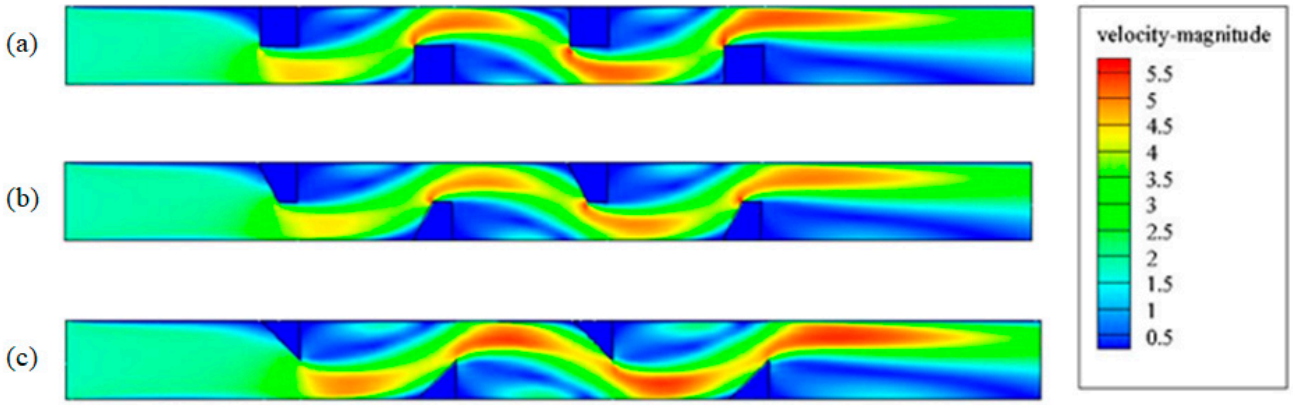

Figure 8. Contours of mean velocity fields for Re = 2500 and different obstacle: (**a**) $\theta = 0°$: square obstacle; (**b**) $0° < \theta < 45°$: trapezoidal obstacle; and (**c**) $\theta = 45°$: triangular obstacle.

According to the average intensity of the velocity, different zones are identified in the three models under investigation (low or high). Just upstream of the first obstacle, the average velocities for the three models under study are low. Along the downstream side of square, trapezoidal, and triangular obstacles, they are also weak. For the three models under study, the average velocities are very high under both the upper and lower obstacle.

The distribution of the average velocity as a function of the Reynolds number is shown in Figure 9. Keep in mind that the average velocity increases as the Reynolds number increases. Additionally, we discover that for Reynolds values 2000–6000, the average velocity in the three instances was quite similar. Reynolds number 6000 indicates that the average velocity dropped in the case of the triangular obstacle and stayed constant in the situations of the square and trapezoidal obstacles.

For the square, trapezoidal, and triangular examples under study, the fluctuation of the axial velocity is depicted in Figure 10. As a result of the obstacle, it can be seen that the flow is actually accelerated. For the flow's perfect straightening upstream of a triangular obstacle, axial velocity is crucial. Velocity is affected in the case of the trapezoidal obstacle. However, because of the vortex that is created in the square case, the velocity varies.

At x = 0.07 m and for various values of the Reynolds number in each of the cases taken into consideration, Figure 11 shows the fluctuation of the axial velocity as a function of the height of the channel. When the channel height is between 0 and 0.015 m, it is shown that the velocity increases, and that the velocity increases as the value of the Reynolds number increases. If we use a Reynolds number to examine the axial velocity profiles for the three models, we find that the square and trapezoidal obstacle models have nearly identical velocities.

For the model with triangle obstacles, the velocities take substantial values. The velocities are observed to be in the opposite direction of the flow at a height of 0.015 m, and the model with triangular obstacles has the highest values of velocities when compared to the other models (Figure 12).

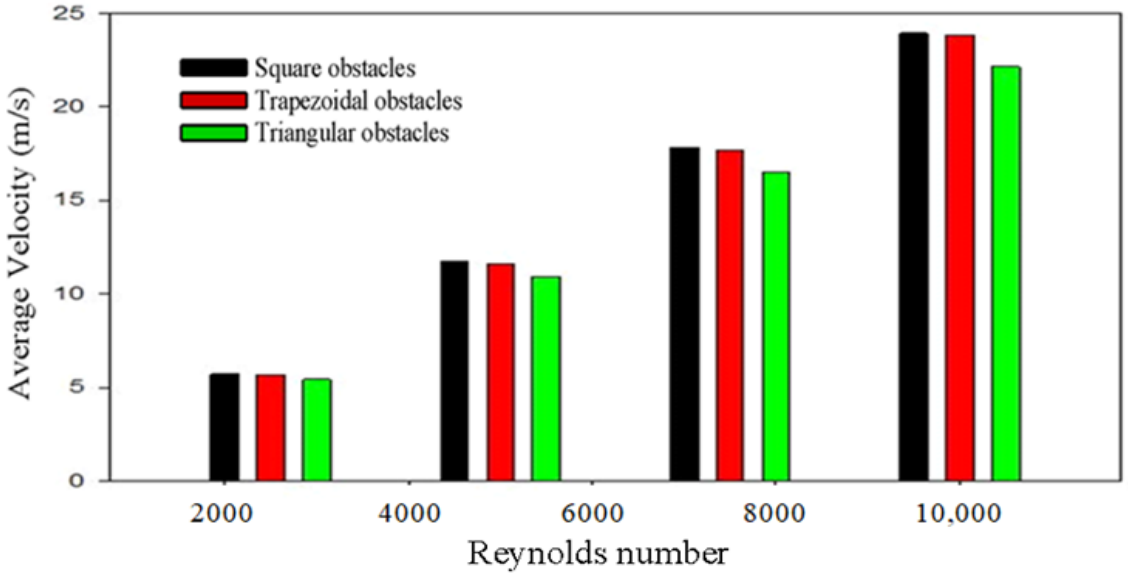

Figure 9. Average velocity as a function of the Reynolds number in the three cases: square, trapezoidal, and triangular.

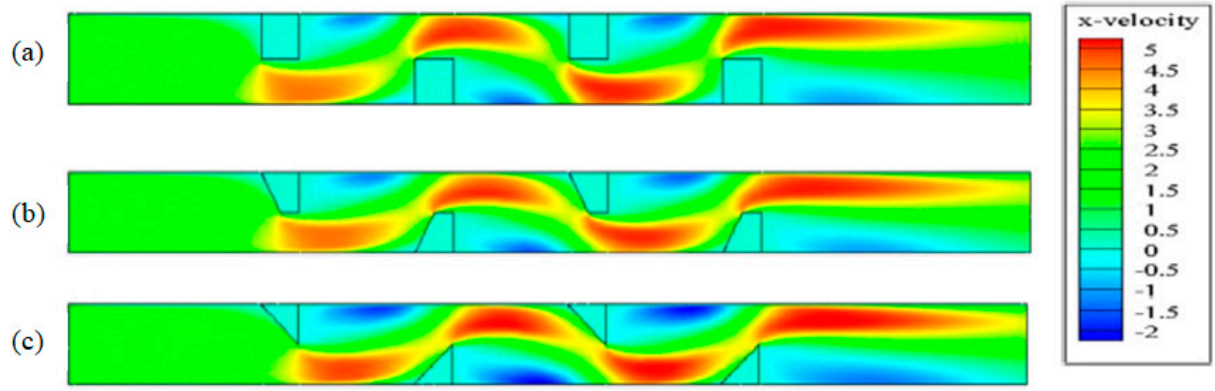

Figure 10. Contours of the axial velocity fields for Re = 2500 and different angles of obstacles: (**a**) $\theta = 0°$: square obstacle; (**b**) $0° < \theta < 45°$: trapezoidal obstacle; and (**c**) $\theta = 45°$: triangular obstacle.

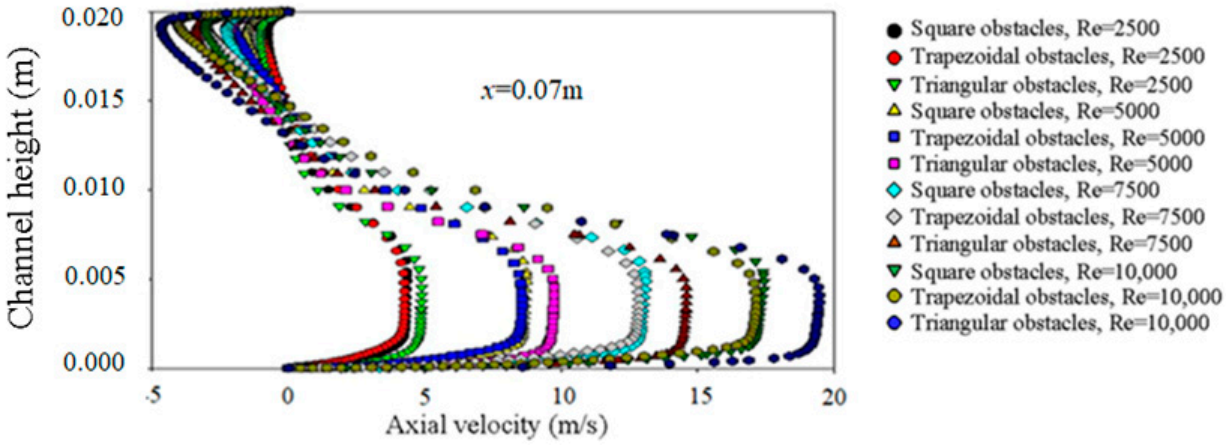

Figure 11. Profiles of the axial velocity, u, downstream of the first obstacle at x = 0.07 m for different angles of obstacles and various values of the Reynolds number.

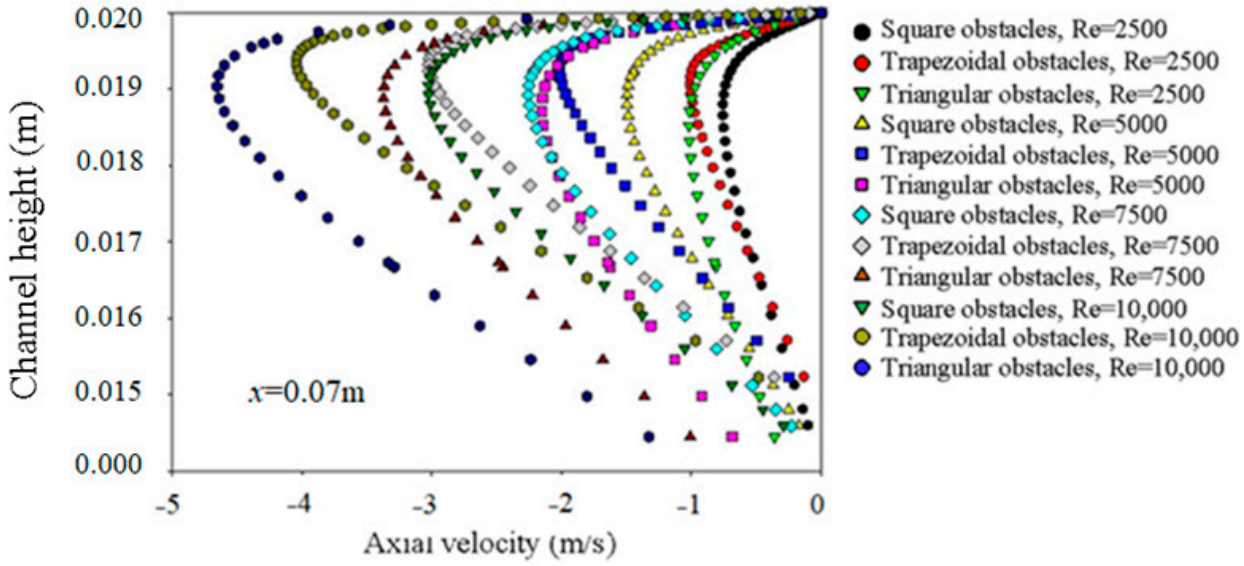

Figure 12. Profiles of the axial velocity for different angles of obstacles and various values of the Reynolds number.

The profiles of the ratios (u/U_{in}) at the channel's outflow ($x = L$) are shown in Figure 13. These profiles demonstrate that for the smallest Reynolds number, Re = 2500, the ratios (u/U_{in}) are similar. The ratios (u/U_{in}) (at the point 0 up to 0.01 m) of the model with a triangular obstacle are low for the maximum Reynolds number, Re = 10,000. For the square obstacle, the model has high ratios (u/U_{in}). The model with a triangular obstacle has large ratios (u/U_{in}) at positions 0.01 to 0.018 m.

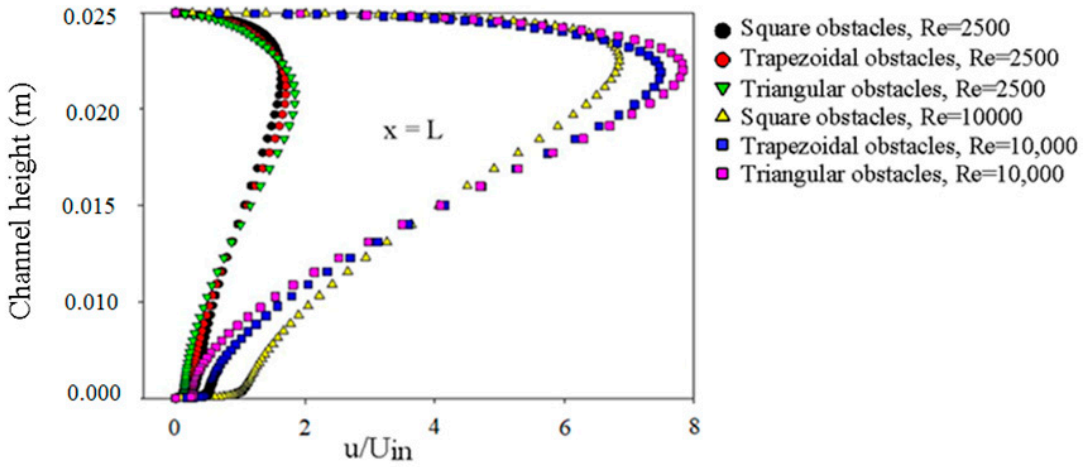

Figure 13. Dimensionless axial velocity profiles (u/U_{in}) at the channel outlet ($x = L$), for different hydrodynamic ($2500 \leq Re \leq 10{,}000$) and geometric ($0° \leq \theta \leq 45°$) parameters.

For the square obstacle, the model has low ratios (u/U_{in}). The other heights (u/U_{in}) for the three models range from 0.018 to 0.02 m. The fluid is viscous, thus when close to the wall, the velocity is zero. Due to the constant section and the varied flow, the various Reynolds numbers result in a variation in velocity.

The change in average axial velocity for the three examples is shown in Figure 14 as a function of Reynolds number. As can be seen, the axial velocity increases as the Reynolds number increases. However, the three investigations revealed an increase in axial velocity. When the Reynolds number is between 2000 and 4000, the velocity value is roughly constant at 5 m/s.

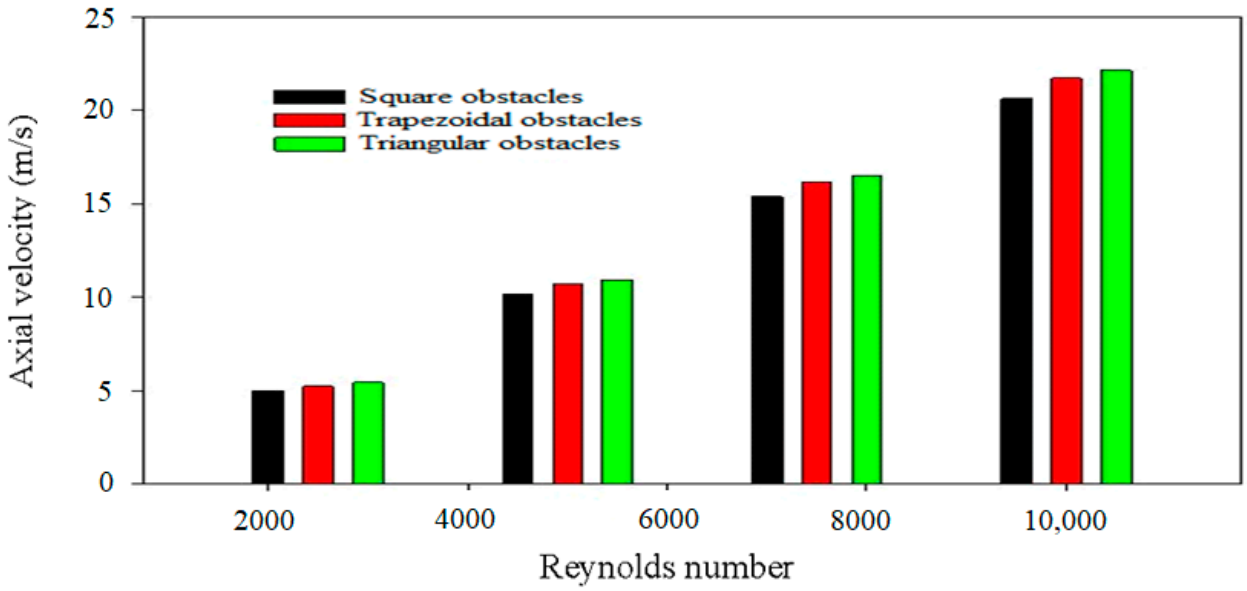

Figure 14. Maximum axial speeds for the different cases studied.

From the value of the Reynolds number 4000, it can be seen that the three examples have different velocities, with the triangular obstacle having the smallest increase in velocity, followed by the trapezoidal obstacle, and then the square obstacle.

Figure 15 shows how the vertical (transverse) velocity varies in the three cases of the triangle, trapezoid, and square. With the exception of the head of the obstacles, the transverse velocity is homogeneous throughout the duct of the channel. However, at the left extremities of the upper and lower obstacles, the velocity assumes positive and negative values, respectively. Upstream of a square obstacle, the velocity is high because of the abrupt pipe section reduction.

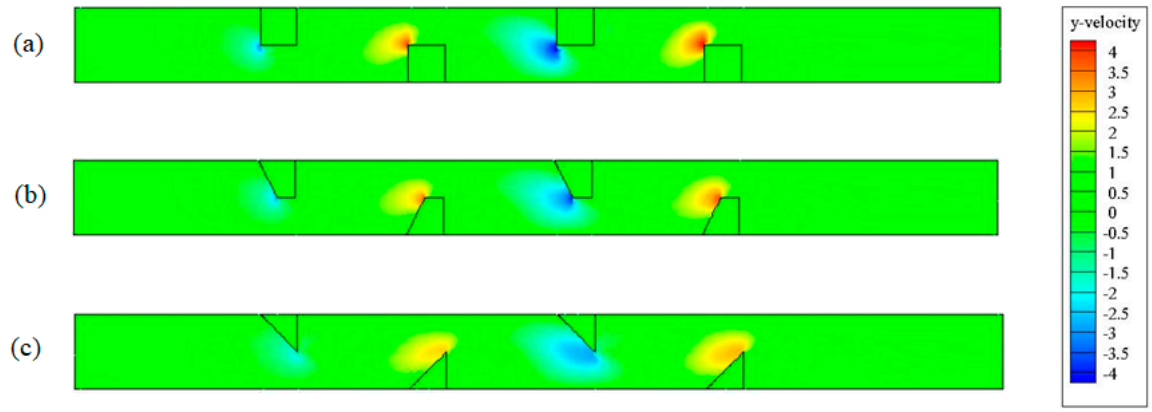

Figure 15. The transverse velocity field in the three cases: (**a**) square, (**b**) trapezoidal and (**c**) triangular, for Re = 2500.

The straightening of the flow causes a trapezoidal obstacle to reduce velocity. Due to the consistent convergence of the channel segment in the event of a triangular obstacle, the velocity is low.

For various shapes of obstacles, Figure 16 illustrates how the maximum transverse velocity varies as a function of the Reynolds number. The velocity rises as the Reynolds number rises. Due to the acute deformation of the pipe section, which results in a vertical translation of the fluid particles, the square shape has the fastest velocity. Due to the low flow convergence, the trapezoidal form moves slower than the square impediment.

Compared to other obstacle forms, the triangle shape moves at a slower speed, which reduces the vertical component of velocity by half.

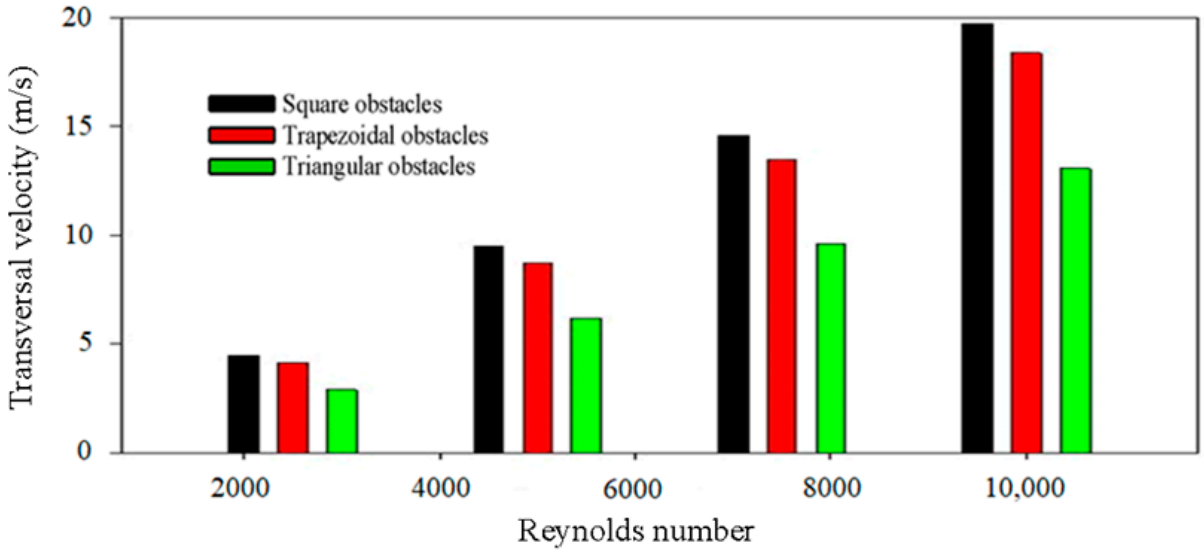

Figure 16. Transverse velocity for different Reynolds numbers in the three cases: square, trapezoidal, and triangular.

The temperature field is depicted in Figure 17. Forced convection causes the air near the absorber to heat up quickly the secondary air in the lower part of the channel downstream of the upper obstacles in Zone A; this suggests that the temperature is high for the three models under consideration. It has been shown that the square obstacle's weak flow recirculation results in minimal contact between the cold air and the obstacle. Due to the obstacle's diversion of the flow in the trapezoidal cases, we see that there is good turbulence. We obtain good cooling in the triangular instance because the interaction between the cold air and the impediment is significant downstream of the obstacle.

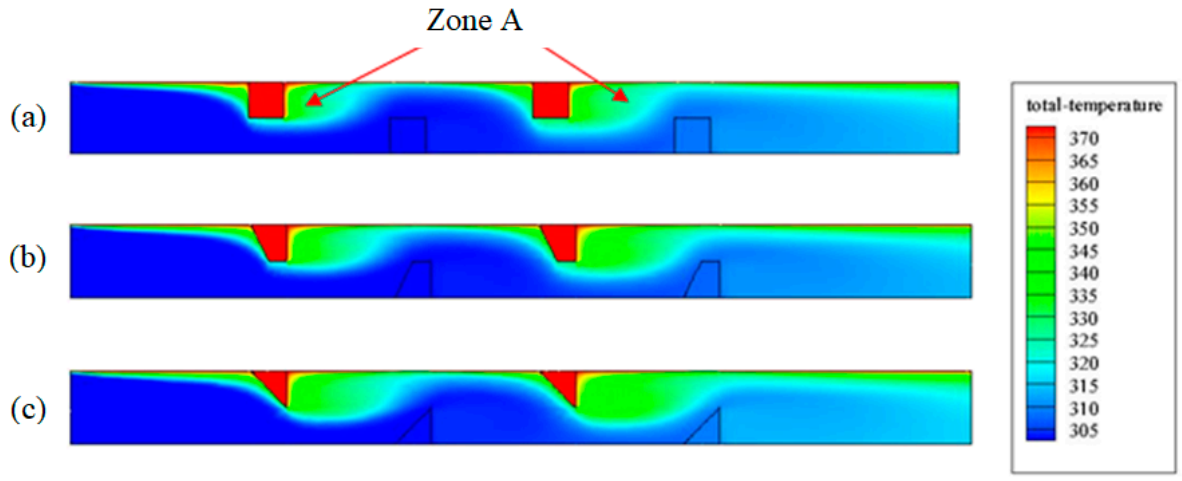

Figure 17. The field of the transverse temperature in the three cases: (**a**) square, (**b**) trapezoidal, and (**c**) triangular for Re = 2500.

The temperature change at the channel's exit is shown in Figure 18 for a range of Reynolds number values and obstacle types. With increasing pipe height, the fluid temperature profile rises exponentially with a different curve for each value of the Reynolds number. Due to the substantial heat flux that heats the surface, the triangle obstacle has the maximum heat transfer. The temperature value at the middle of two configurations

is what causes the trapezoidal obstacle to have an average heat flow (between square and triangular). Due to the cooling air temperature, the square obstacle has the weakest heat transmission (poor cooling). It can be concluded that the temperature values of the model channel with triangle obstacles are very high. The three models' temperatures are comparable when the Reynolds number is raised to 10,000.

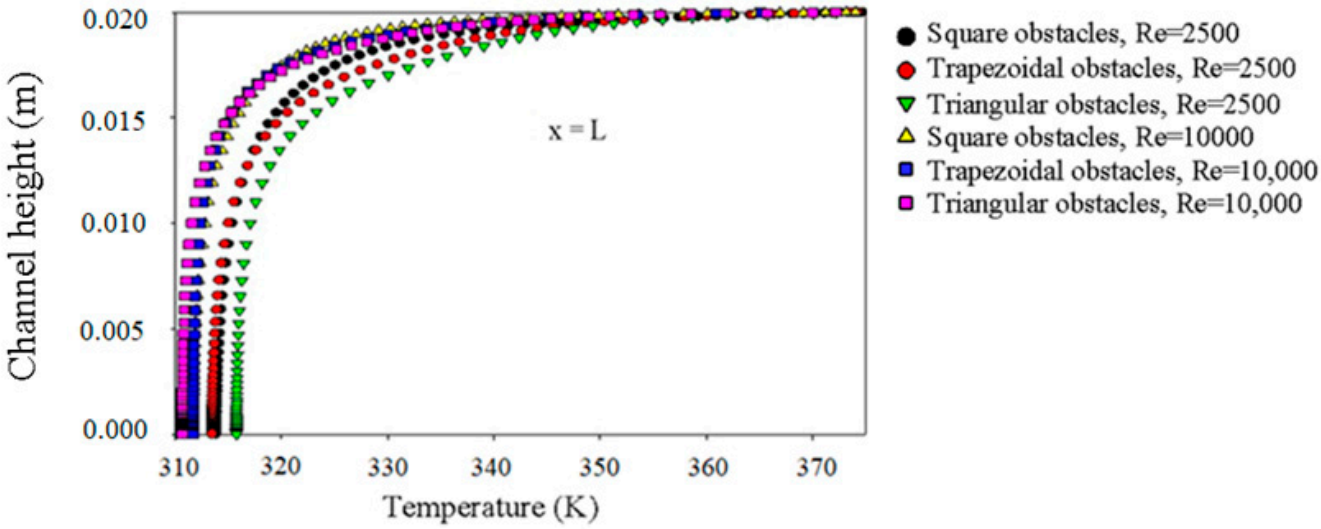

Figure 18. Temperature profile at the outlet of channel in the three cases: square, trapezoidal, and triangular.

Figure 19 shows how the square, trapezoidal, and triangular shapes of obstacles affect the evolution of the adimensional Nusselt ratio (Nu_x/Nu_0) with channel length. Depending on the width of the channel, the Nusselt number fluctuates sinusoidally between obstacles.

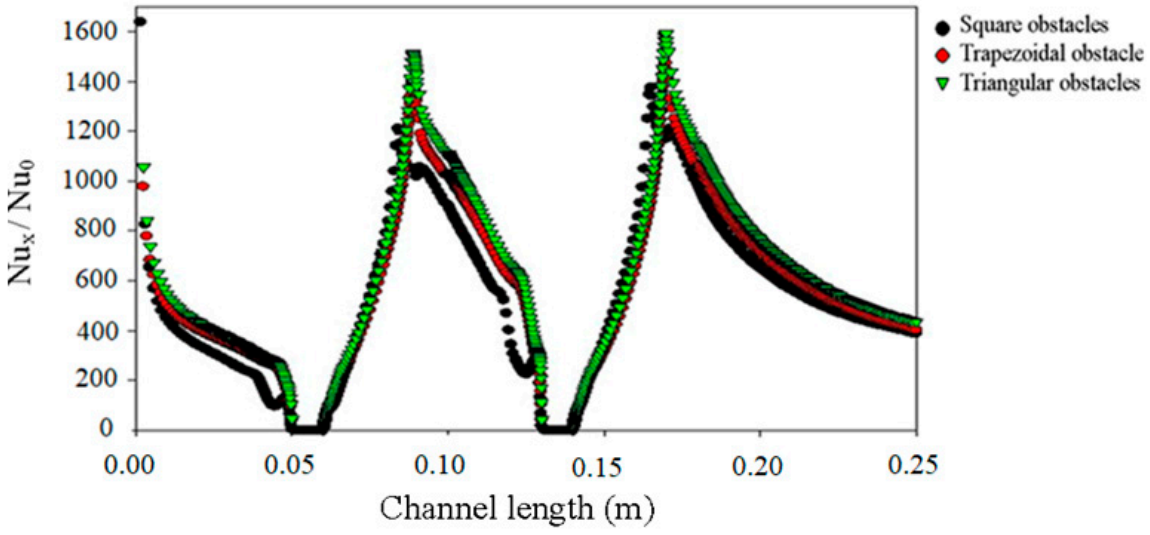

Figure 19. The normalized local Nusselt number (Nu_x/Nu_0) along the channel in the three cases: square, trapezoidal, and triangular for *Re* = 2500.

The turbulence of the flow results in increased convective heat transfer, which is illustrated in the picture as having a significant value for the Nusselt number in the case of the triangle obstacle. As the heat flow is blended in the trapezoidal enclosure, the heat transfer is better (a solid part and a fluid part). As there is more heat transfer in the solid in the square example, the Nusselt number is low, emphasizing the significance

of conduction. The important values in the model with triangle obstacles are used to calculate the normalized local Nusselt number; the value of the ratio (Nu_x/Nu_0) reaches a maximum of 1600 at the 0.17 m position. This explains why the model with triangle obstacles had better heat transfer than the other models analyzed.

The change in the average normalized Nusselt number (Nu_x/Nu_0) as a function of the Reynolds number for various obstacle forms is shown in Figure 20. It has been noted that as the Reynolds number rises, the average Nusselt value also rises (convection is important for a high Reynolds value, and conduction is almost zero for high velocities). The high axial velocity produces a higher convection force than the other examples, by increasing the fluid's recirculation zones, as shown in the picture, which demonstrates that the Nusselt number has a considerable value in the case of the triangle obstruction. The Nusselt number is smaller for the trapezoidal obstacle because the shape itself creates the restriction to the flow. Due to the geometry of the impediment blocking flow velocity in the square case, the Nusselt number is low.

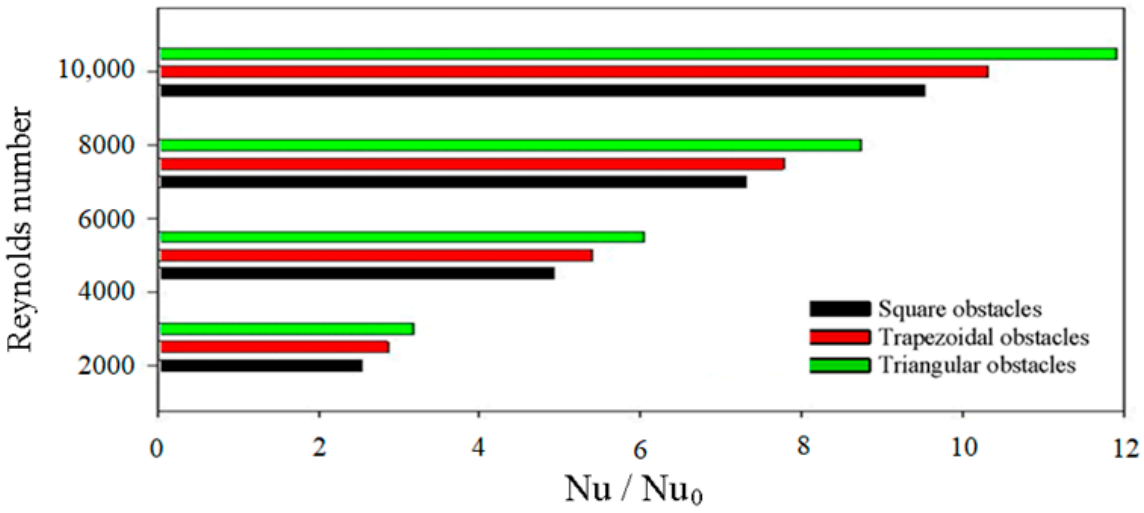

Figure 20. Average Nusselt number (Nu/Nu_0) along the hot wall (upper wall) for different Re numbers in the three cases: square, trapezoidal, and triangular.

Over the course of the channel's whole hot length, Figure 21 depicts the local variation of the friction coefficient's adimensional ratio $\left(C_f/f_0\right)$. Only at the level of the obstacles does the coefficient of friction rise. The figure demonstrates that for the square obstacle, the friction coefficient has a high value. At a distance of 0.19 m, the value of $\left(C_f/f_0\right)$ can be as high as 4800. The average value of the coefficient of friction is zero due to the flow's straightening. As the air flow is homogeneous in the triangular example, the coefficient of friction is low.

This shows how the physical characteristics of the fluid flow, the increase in heat transfer rate resulting from the decrease in the local coefficient of friction, are strongly influenced by the geometry of the obstacles.

Figure 22 illustrates the evolution of the friction ratio (f/f_0) according to the different values of the Reynolds number for different obstacle models. On the other hand, it is seen that for the three models examined, the average coefficient of friction rises as the Reynolds number rises. When comparing the models for a given Reynolds number, we see that the average coefficient of friction values for the model with square obstacles are crucial due to the significant turbulence they produce. However, because of air recirculation, the average coefficient of friction values for the model with triangular obstacles are low.

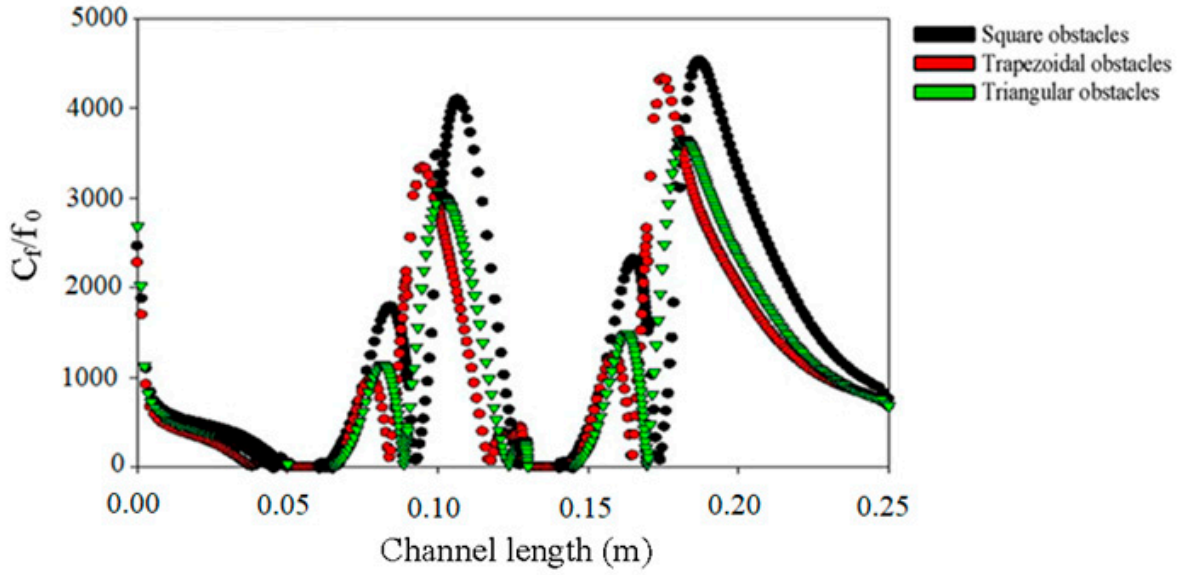

Figure 21. The profile of the local friction coefficient $\left(C_f / f_0\right)$ along the channel (upper wall) in the three cases: square, trapezoidal, and triangular for *Re* = 2500.

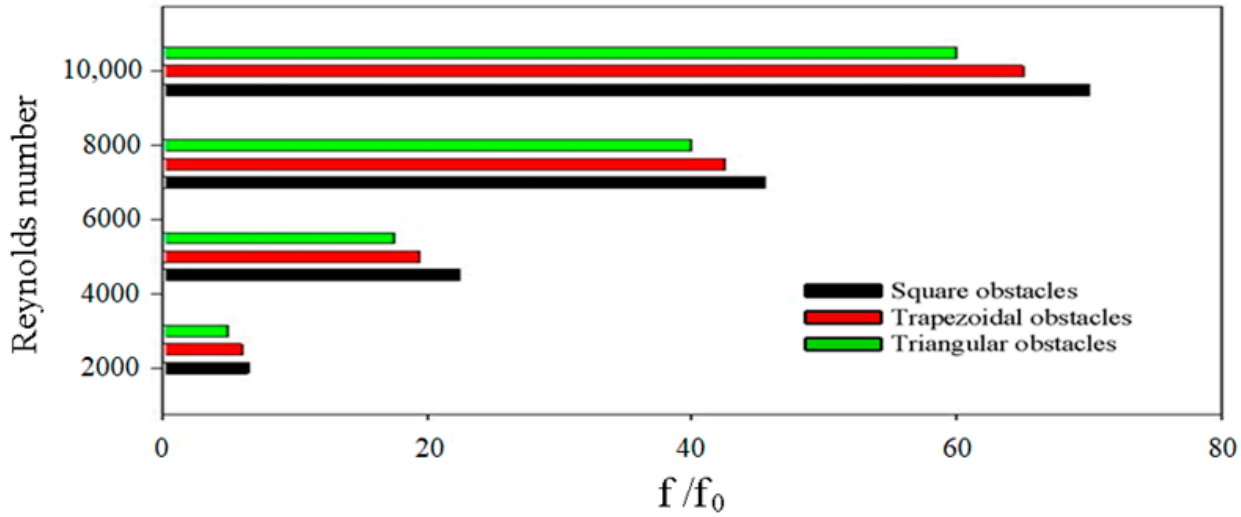

Figure 22. Average coefficient of friction (f / f_0) at different numbers of Re along the hot wall (upper wall) in the three cases: square, trapezoidal, and triangular.

To enhance heat transmission between the absorber and the heat transfer fluid, the researched roughnesses of square and triangular Type 1, Type 2, and Type 3 are situated on the hot top part of the channel (absorber), downstream of the second baffle. In the presence of triangular obstacles, Figure 23 shows the distribution of the average velocity as a function of the shape of the roughness (square roughness and triangle roughness). Due to the driving surface's unprofiled deformation, the average velocity in the case of square roughness is insignificant. As the subsequent profile lies downstream of the triangular roughness (Type 1), the average speed is low at the beginning of the roughness. Due to the flow profiling discontinuities with the triangular roughness (Type 2), the average velocity is relatively high. The average velocity has a significant value when there is triangular roughness (Type 3).

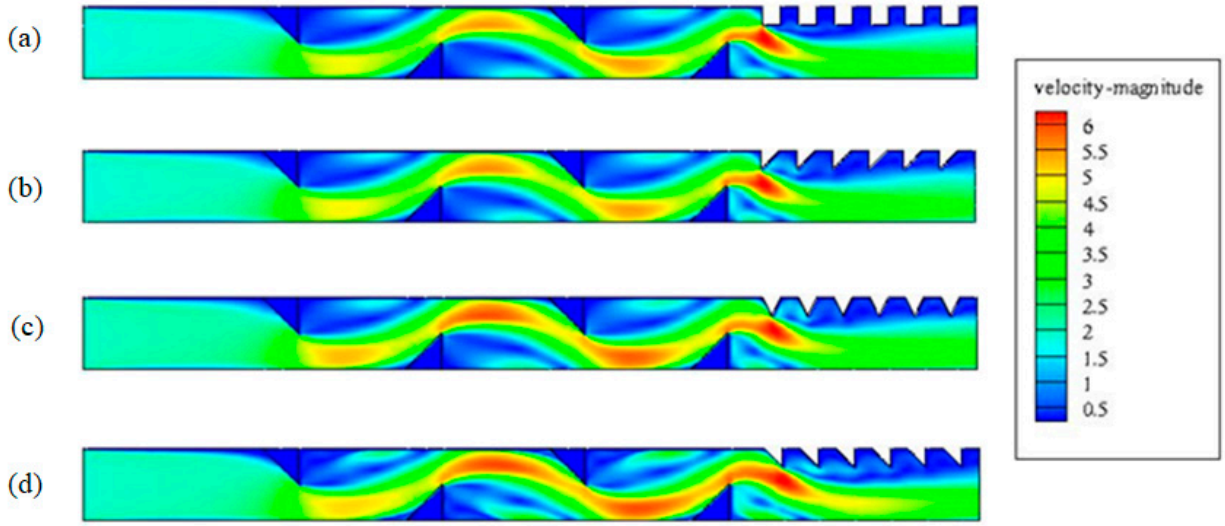

Figure 23. Average velocity fields in the four cases of roughness, (**a**) square roughness, (**b**) triangular roughness Type 1, (**c**) triangular roughness Type 2, and (**d**) triangular roughness Type 3 for *Re* = 2500.

Figure 24 displays the temperature distribution for each of the four proposed models for the roughness, fin presence, and triangle baffles across the entire examined region. The temperature is quite high where the absorber and obstacles are located, as well as in the roughness asperities. The channel's exit is improved by the addition of roughness. Due to inadequate air recirculation at the roughness's center, the fluid temperature field has low cooling effectiveness in the case of square roughness. Due to the airflow being inserted into the triangle roughness Type 1, the channel has effective cooling. Due to the good curvature of the triangle roughness Type 2, the temperature field has good agitation in the region. Due to the best heat flow straightening provided by triangle roughness Type 3, the temperature field has ideal cooling in this scenario.

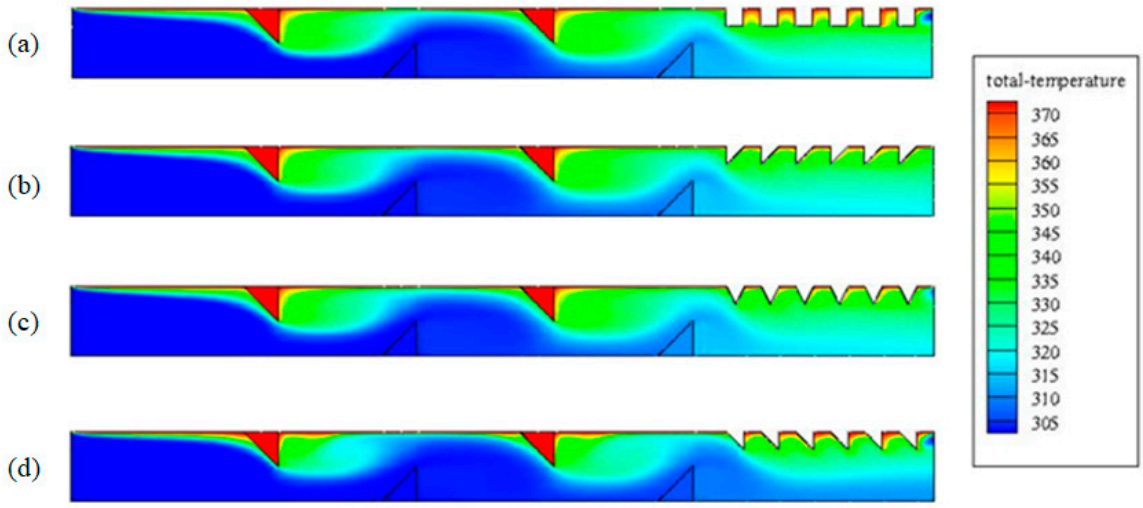

Figure 24. The temperature field in the four cases of roughness: (**a**) square roughness, (**b**) triangular roughness Type 1, (**c**) triangular roughness Type 2, and (**d**) triangular roughness Type 3 for *Re* = 2500.

For each of the several situations of roughness considered for the air duct with triangular fins, Figure 25 shows the fluctuations in values of normalized average Nusselt number (Nu/Nu_0) as a function of the Reynolds number. With an increase in Reynolds number comes an increase in the mean Nusselt number, and high velocity produces high convection.

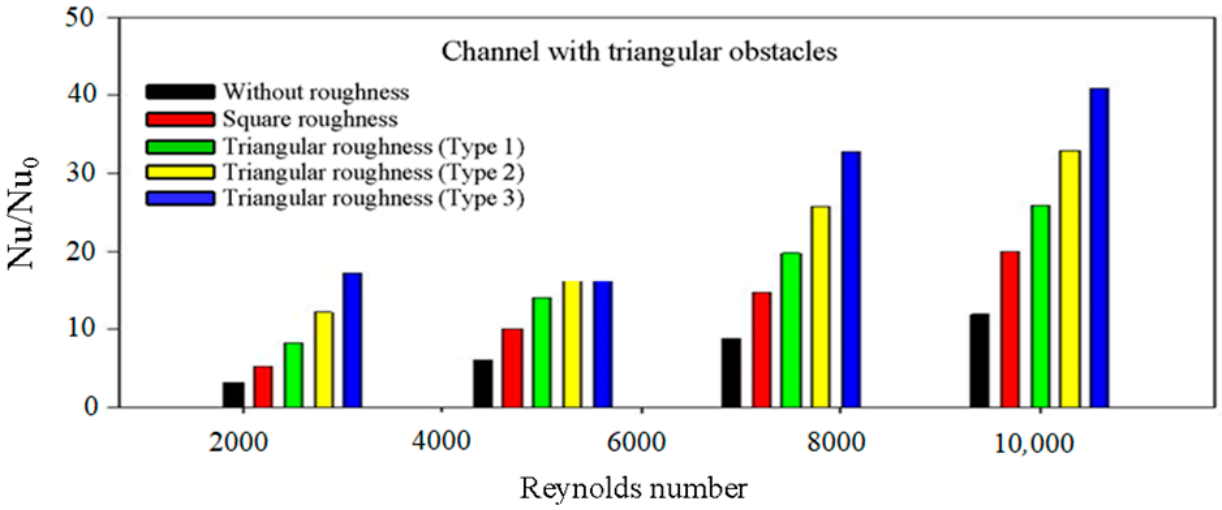

Figure 25. Normalized average Nusselt number (Nu/Nu_0) as a function of the Reynolds number in various roughnesses.

Due to the flow's effective guidance, the figure demonstrates that the average Nusselt number is large in the case of triangular roughness Type 3. Due to the regular separation of the flow, the Nusselt number is decreased in the case of triangular roughness Type 2.

Because the attack surface has straight roughness in the case of triangular roughness Type 1, the Nusselt number is low. Due to inadequate fluid recirculation, the Nusselt number in the case of square roughness is minimal. The exchange surface is low in the absence of roughness, which causes a very noticeable fall in the Nusselt values.

For four various types of roughness, including square and triangular roughness, Figure 26 depicts the evolution of the average ratio (f/f_0) as a function of the Reynolds number, which ranges between 2500 and 10,000 (Types 1, 2, and 3). As Reynolds number rises, the average coefficient of friction rises as well. As there is a huge contact surface in the case of square roughness, the figure demonstrates that the average coefficient of friction has a high value. Moreover, as the triangular roughness Type 1 is perpendicular to the flow direction, the coefficient of friction is lower. Due to the minimal flow disturbance in the case of a triangular roughness Type 2, the coefficient of friction is lower. The low flow resistance in the case of a triangular roughness Type 3 lowers the coefficient of friction. When there is no roughness, the coefficient of friction is low because the flow cannot be impeded.

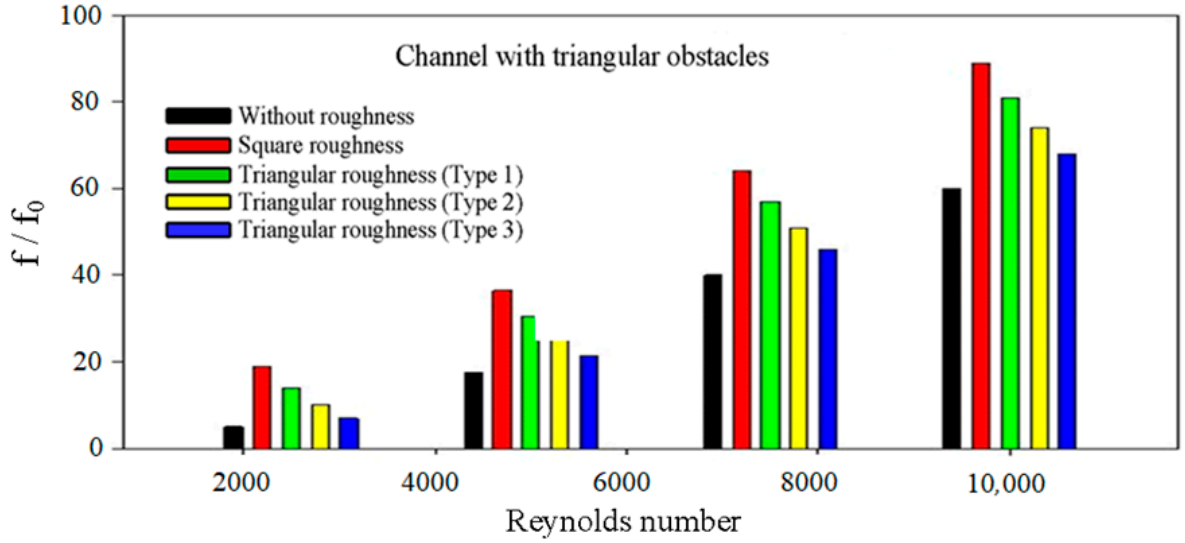

Figure 26. The average coefficient of friction for various numbers of *Re* in various situations.

4. Conclusions

In this article, we presented a numerical study of forced convection cooling of a microprocessor in a channel with obstacles and roughness. The main goal of this study is to provide a better understanding of this phenomenon, while also reflecting on more diverse cooling techniques and getting as close as possible to actual usage conditions.

During our study, we used the fluent computer code ANSYS as well as its gambit mesh generator on several cases, which allowed us to become more familiar with numerical simulation. The complexity of the geometric configuration has been mastered by the gambit, but the shape intended for us is relatively complicated to achieve and to knit, which requires quality and, above all, precise work. The importance of digital investigation is to shed light on the physical phenomena described by the theory without physical experience, which is more expensive.

- Several parameters are studied, in particular the hydrodynamic ($2500 \leq Re \leq 10{,}000$) and geometric ($0\ ^\circ \leq \theta \leq 45^\circ$) parameters.
- The three types of obstacle: $\theta = 0^\circ$: square obstacle; $0^\circ < \theta < 45^\circ$: trapezoidal obstacle; and $\theta = 45^\circ$: triangular obstacle, with $Re = 2500$, generate complex phenomena such as recirculation zones and turbulence regions upstream and downstream of the obstacles and a turbulent zone for the model containing triangular obstacles is very important compared to other models.
- The upstream sharp edge has a point of separation (wall of the obstacle) where the dynamic pressure is very high, which causes a depression downstream of these obstacles.
- For a triangular obstacle the pressure has a significant value, which gave us a tremendous movement.
- The higher the Reynolds number, the greater the dynamic pressure.
- For Reynolds values between 2500 and 6000, the average velocity for the three cases (square, trapezoidal, and triangular obstacle) was extremely close.
- In the case of a triangular obstacle, the contact between the cold air and the obstacle is important downstream of the obstacle, which gives us good cooling, and the Nusselt number has an important value, because the agitation of the flow gives us more convective heat transfer and the coefficient of friction is low because the air flow is uniform.
- The comparative study among the four models of the triangular Type 1, triangular Type 2, and triangular Type 3 channels shows that in the case of a triangular roughness Type 3 the average velocity has a great value.
- In the case of a triangle roughness Type 3 channel, the average velocity has a considerable value, according to the comparative study using the four models for triangular Type 1, triangular Type 2, and triangular Type 3 channels.
- The temperature field has perfect cooling, because of the best straightening of the heat flux by this roughness;
- The average Nusselt number has a high value;
- The coefficient of friction is lowered, because the flow resistance is low.

Author Contributions: Conceptualization, A.B. and R.R.; methodology, R.R. and A.B.; software, M.A., R.R. and A.B.; validation, A.B. and R.R.; formal analysis, A.B., R.R. and M.A.; investigation, A.B. and R.R.; resources, A.B., R.R. and M.A.; data curation, A.B. and M.A.; Funding, A.B. and R.R.; writing-original draft preparation, A.B. and R.R.; writing-review and editing, A.B., R.R. and M.A. All authors have read and agreed to the published version of the manuscript.

Funding: This research received no external funding.

Data Availability Statement: The data that support the findings of this study are available from the corresponding author upon reasonable request.

Conflicts of Interest: The authors declare no conflict of interest.

References

1. Kumar, A.; Kim, M.H. Convective heat transfer enhancement in solar air channels. *Appl. Therm. Eng.* **2015**, *89*, 239–261. [CrossRef]
2. Liu, J.; Gao, J.; Gao, T.; Shi, X. Heat transfer characteristics in steam-cooled rectangular channels with two opposite rib-roughened walls. *Appl. Therm. Eng.* **2013**, *50*, 104–111. [CrossRef]
3. Ali, M.; Zeitoun, O.; Nuhait, A. Forced convection heat transfer over horizontal triangular cylinder in cross flow. *Int. J. Therm. Sci.* **2011**, *50*, 106–114. [CrossRef]
4. Kumar, A.; Bhagoria, J.L.; Sarviya, R.M. Heat transfer and friction correlations for artificially roughened solar air heater duct with discrete W-shaped ribs. *Energy Convers. Manag.* **2009**, *50*, 2106–2117. [CrossRef]
5. Karwa, R.; Maheshwari, B.K.; Karwa, N. Experimental study of heat transfer enhancement in an asymmetricallyheated rectangular duct with perforated baffles. *Int. Commun. Heat Mass Transf.* **2005**, *32*, 275–284. [CrossRef]
6. Kabeel, A.E.; Hamed, M.H.; Omara, Z.M.; Kandeal, A.W. Influence of fin height on the performance of a glazed and bladed entrance single-pass solar air heater. *Sol. Energy* **2018**, *162*, 410–419. [CrossRef]
7. Demartini, L.C.; Vielmo, H.A.; Moller, S.V. Numeric and Experimental Analysis of The Turbulent Flow Through a Channel with Baffle Plates. *J. Braz. Soc. Mech. Sci. Eng.* **2004**, *26*, 153–159. [CrossRef]
8. Cao, X.; Du, T.; Liu, Z.; Zhai, H.; Duan, Z. Experimental and numerical investigation on heat transfer and fluid flow performance of sextant helical baffle heat exchangers. *Int. J. Heat Mass Transf.* **2019**, *142*, 118437. [CrossRef]
9. Saedodin, S.A.H.Z.S.; Zamzamian, S.A.H.; Nimvari, M.E.; Wongwises, S.; Jouybari, H.J. Performance evaluation of a flat-plate solar collector filled with porous metalfoam: Experimental and numerical analysis. *Energy Convers. Manag.* **2017**, *153*, 278–287. [CrossRef]
10. Abchouyeh, M.A.; Fard, O.S.; Mohebbi, R.; Sheremet, M.A. Enhancement of heat transfer of nanofluids in the presence of sinusoidal side obstacles between two parallel plates through the lattice Boltzmann method. *Int. J. Mech. Sci.* **2019**, *156*, 159–169. [CrossRef]
11. Chompookham, T.; Thianpong, C.; Kwankaomeng, S.; Promvonge, P. Heat transfer augmentation in a wedge-ribbed channel using winglet vortex generators. *Int. Commun. Heat Mass Transf.* **2010**, *37*, 163–169. [CrossRef]
12. Dutta, P.; Hossain, A. Internal cooling augmentation in rectangular channel using two inclined baffles. *Int. J. Heat Fluid Flow* **2005**, *26*, 223–232. [CrossRef]
13. Kalaiarasi, G.; Velraj, R.; Swami, M.V. Experimental energy and exergy analysis of a flat plate solar air heater with a new design of integrated sensible heat storage. *Energy* **2016**, *111*, 609–619. [CrossRef]
14. Peng, D.; Zhang, X.; Dong, H.; Lv, K. Performance study of a novel solar air collector. *Appl. Therm. Eng.* **2010**, *30*, 2594–2601. [CrossRef]
15. Selimefendigil, F.; Oztop, H.F.; Sheremet, M.A.; Abu-Hamdeh, N. Forced convection of Fe3O4-water nanofluid in a bifurcating channel under the effect of variable magnetic field. *Energies* **2019**, *12*, 666. [CrossRef]
16. Kamali, R.; Binesh, A.R. The importance of rib shape effects on the local heat transfer and flow friction characteristics of square ducts with ribbed internal surfaces. *Int. Commun. Heat Mass Transf.* **2008**, *35*, 1032–1040. [CrossRef]
17. Siddiqui, M.K. Heat transfer augmentation in a heat exchanger tube using a baffle. *Int. J. Heat Fluid Flow* **2007**, *28*, 318–328.
18. Wang, F.; Zhang, J.; Wang, S. Investigation on flow and heat transfer characteristics in rectangular channel with drop-shaped pin fins. *Propuls. Power Res.* **2012**, *1*, 64–70. [CrossRef]
19. Eiamsa-ard, S.; Promvonge, P. Numerical study on heat transfer of turbulent channel flow over periodic grooves. *Int. Commun. Heat Mass Transf.* **2008**, *35*, 844–852. [CrossRef]
20. Ozceyhan, V.; Gunes, S.; Buyukalaca, O.; Altuntop, N. Heat transfer enhancement in a tube using circular cross sectional rings separated from wall. *Appl. Energy* **2008**, *85*, 988–1001. [CrossRef]
21. Promvonge, P.; Changcharoen, W.; Kwankaomeng, S.; Thianpong, C. Numerical heat transfer study of turbulent square-duct flow through inline V-shaped discrete ribs. *Int. Commun. Heat Mass Transf.* **2011**, *38*, 1392–1399. [CrossRef]
22. Sripattanapipat, S.; Promvonge, P. Numerical analysis of laminar heat transfer in a channel with diamond-shaped baffles. *Int. Commun. Heat Mass Transf.* **2009**, *36*, 32–38. [CrossRef]
23. Yang, Z. Large-eddy simulation: Past, present and the future. *Chin. J. Aeronaut.* **2015**, *28*, 11–24.
24. De Vanna, F.; Bernardini, M.; Picano, F.; Benini, E. Wall-modeled LES of shock-wave/boundary layer interaction. *Int. J. Heat Fluid Flow.* **2022**, *98*, 109071. [CrossRef]
25. Pirouz, M.M.; Farhadi, M.; Sedighi, K.; Nemati, H.; Fattahi, E. Lattice Boltzmann simulation of conjugate heat transfer in a rectangular channel with wall-mounted obstacles. *ScientiaIranica* **2011**, *18*, 213–221.
26. Mohammadi, K.; Sabzpooshani, M. Comprehensive performance evaluation and parametric studies of single pass solar air heater with fins and baffles attached over the absorber plate. *Energy* **2013**, *57*, 741–750. [CrossRef]
27. Skullong, S.; Thianpong, C.; Jayranaiwachira, N.; Promvonge, P. Experimental and numerical heat transfer investigation in turbulent square-duct flow through oblique horseshoe baffles. *Chem. Eng. Process. Process Intensif.* **2016**, *99*, 58–71. [CrossRef]
28. Priyam, A.; Chand, P. Thermal and thermohydraulic performance of wavy finned absorber solar air heater. *Sol. Energy* **2016**, *130*, 250–259. [CrossRef]
29. Hu, J.; Sun, X.; Xu, J.; Li, Z. Numerical analysis of mechanical ventilation solar air collector with internal baffles. *Energy Build.* **2013**, *62*, 230–238. [CrossRef]

30. Amraoui, M.A.; Aliane, K. Three-dimensional analysis of air flow in a flat plate solar collector. *Period. Mech. Eng.* **2018**, *62*, 126–135. [CrossRef]
31. Amraoui, M.A. Numerical Study of an Air Flow in a Flat Plate Air Solar Collector with Circular Obstacles. In *International Conference in Artificial Intelligence in Renewable Energetic Systems*; Springer: Cham, Switzerland, 2020; pp. 839–846.
32. Amraoui, M.A. Three-Dimensional Numerical Simulation of a Flat Plate Solar Collector with Double Paths. *Int. J. Heat Technol.* **2021**, *39*, 1087–1096. [CrossRef]
33. Amraoui, M.A.; Benosman, F. Numerical modeling of a flat air solar collector fitted with obstacles. In Proceedings of the E3S Web of Conferences, Paris, France, 18–21 May 2021; EDP Sciences: Lejulis, France, 2021; Volume 321, p. 04016.
34. Leonardi, S.; Orlandi, P.; Djenidi, L.; Antonia, R.A. Structure of turbulent channel flow with square bars on one wall. *Int. J. Heat Fluid Flow* **2004**, *25*, 384–392. [CrossRef]
35. Miyake, Y.; Tsujimoto, K.; Nakaji, M. Direct numerical simulation of rough-wall heat transfer in a turbulent channel flow. *Int. J. Heat Fluid Flow* **2001**, *22*, 237–244. [CrossRef]
36. Ansari, M.; Bazargan, M. Optimization of flat plate solar air heaters with ribbed surfaces. *Appl. Therm. Eng.* **2018**, *136*, 356–363. [CrossRef]
37. Kim, K.Y.; Kim, S.S. Shape optimization of rib-roughened surface to enhance turbulent heat transfer. *Int. J. Heat Mass Transf.* **2002**, *45*, 2719–2727. [CrossRef]
38. Jang, Y.J.; Chen, H.C.; Han, J.C. Computation of flow and heat transfer in two-pass channels with 60 deg ribs. *J. Heat Transf.* **2001**, *123*, 563–575. [CrossRef]
39. Kim, H.M.; Kim, K.Y. Shape optimization of three-dimensional channel roughened by angled ribs with RANS analysis of turbulent heat transfer. *Int. J. Heat Mass Transf.* **2006**, *49*, 4013–4022. [CrossRef]
40. Kumar, R.; Kumar, A.; Goel, V. A parametric analysis of rectangular rib roughened triangular duct solar air heater using computational fluid dynamics. *Sol. Energy* **2017**, *157*, 1095–1107. [CrossRef]
41. Ryu, D.N.; Choi, D.H.; Patel, V.C. Analysis of turbulent flow in channels roughened by two-dimensional ribs and three-dimensional blocks. Part II: Heat transfer. *Int. J. Heat Fluid Flow* **2007**, *28*, 1112–1124. [CrossRef]
42. Liou, T.M.; Hwang, J.J.; Chen, S.H. Simulation and measurement of enhanced turbulent heat transfer in a channel with periodic ribs on one principal wall. *Int. J. Heat Mass Transf.* **1993**, *36*, 507–517. [CrossRef]
43. Alam, T.; Kim, M.H. Heat transfer enhancement in solar air heater duct with conical protrusion roughness ribs. *Appl. Therm. Eng.* **2017**, *126*, 458–469. [CrossRef]
44. Kumar, A.; Layek, A. Energetic and exergetic performance evaluation of solar air heater with twisted rib roughness on absorber plate. *J. Clean. Prod.* **2019**, *232*, 617–628. [CrossRef]
45. Skullong, S.; Promvonge, P.; Thianpong, C.; Jayranaiwachira, N.; Pimsarn, M. Heat transfer augmentation in a solar air heater channel with combined winglets and wavy grooves on absorber plate. *Appl. Therm. Eng.* **2017**, *122*, 268–284. [CrossRef]
46. Deo, N.S.; Chander, S.; Saini, J.S. Performance analysis of solar air heater duct roughened with multigap V-down ribs combined with staggered ribs. *Renew. Energy* **2016**, *91*, 484–500. [CrossRef]
47. Gabhane, M.G.; Kanase-Patil, A.B. Experimental analysis of double flow solar air heater with multiple C shape roughness. *Sol. Energy* **2017**, *155*, 1411–1416. [CrossRef]
48. Kumar, K.; Prajapati, D.R.; Samir, S. Heat transfer and friction factor correlations development for solar air heater duct artificially roughened with 'S'shape ribs. *Exp. Therm. Fluid Sci.* **2017**, *82*, 249–261. [CrossRef]
49. Ravi, R.K.; Saini, R.P. Nusselt number and friction factor correlations for forced convective type counter flow solar air heater having discrete multi V shaped and staggered rib roughness on both sides of the absorber plate. *Appl. Therm. Eng.* **2018**, *129*, 735–746. [CrossRef]
50. Launder, B.E.; Spalding, D.B. The numerical computation of turbulence flow. *Comput. Methods Appl. Mech. Eng.* **1974**, *3*, 269–289. [CrossRef]